Journal of Marine Research, 56, 1225–1258, 1998

Small viscosity behavior of a homogeneous, quasi-geostrophic, ocean circulation model

by Robert B. Scott[1,2] and David N. Straub[1]

ABSTRACT

Insensitivity to turbulent closure in the wind-driven nonlinear Stommel-Munk model is addressed theoretically and numerically. The QG energy equation is used to show that, with the assumption that the maximum velocities occur at inertial length scales or smaller, a Sverdrup interior is consistent with the small Rossby number assumption only when the frictional parameters exceed critical values. For frictional parameters smaller than these values, valid solutions must decrease the energy source. This is possible for non-Sverdrup solutions since the energy source is dependent on the solution. The steady-state behavior of the model was investigated via a pseudo-arclength continuation algorithm. Dependence on the boundary layer Reynolds number, *Re*, was investigated by varying the eddy viscosity for fixed wind forcing. A tendency to decrease the energy source was found for solutions that are nonsymmetric about the center latitude. Antisymmetric solutions displayed the opposite behavior and diverged more quickly with increasing *Re*. The robustness of the results to dynamic boundary condition, symmetry and strength of wind stress, time dependence and bottom friction were tested. Some aspects of the nonsymmetric solutions appeared insensitive to *Re*.

1. Introduction

Idealized ocean general circulation models have played an important role in the theoretical understanding of the midlatitude, horizontal ocean circulation observed in various basins of the world ocean. These models are often based on quasi-geostrophic, QG, theory applied to a homogeneous fluid on a β-plane. This reduces the problem to a two-dimensional vorticity equation, see for example Pedlosky (1987). The utility of these models stems in part from their simplicity in that they are intended to be generic. They provide, it is hoped, insight into the important dynamics which can be reduced to a parametric dependence upon observable factors like the strength of the wind. The frictional closure of these models involves parameters of a different kind. The subgrid scale processes are typically modeled with a bottom friction term that parameterizes the bottom Ekman layer, $-r\nabla^2\psi$, for the Stommel model (Stommel, 1948), or a lateral friction term in the form of an eddy viscosity, $A_H\nabla^4\psi$, for the Munk model (Munk, 1950). The combined

1. Department of Atmospheric and Oceanic Sciences, Center for Climate and Global Change Research, McGill University, Montreal, QC, H3A 2K6, Canada.

2. CERCA, Center for Research on Computation and its Applications, 5160 Decarie, Suite 400, Montreal, QC, H3X 2H9, Canada.

nonlinear Stommel-Munk model for a constant depth basin is,

$$\frac{\partial \nabla^2 \psi}{\partial t} + J(\psi, \nabla^2 \psi + \beta y) = \frac{f_o W_E}{H} + A_H \nabla^4 \psi - r \nabla^2 \psi, \tag{1}$$

where ψ is the streamfunction for the QG flow, J is the Jacobian operator with respect to x and y, f_o is the Coriolis parameter, $\beta = \partial f / \partial y$, W_E is the Ekman pumping velocity and H is the depth of the fluid. Four dimensionless parameters completely define the problem: the aspect ratio, the inertial number, the Munk number, and the Stommel number:

$$\alpha \equiv \frac{L_y}{L_x}; \qquad \delta_I \equiv \left(\frac{f_o W}{H \beta^2 L_x^2} \right)^{1/2}; \qquad \delta_M \equiv \left(\frac{A_H}{\beta L_x^3} \right)^{1/3}; \qquad \delta_S \equiv \frac{r}{\beta L_x} \tag{2}$$

where L_x and L_y are the x and y basin dimensions, W is the maximum of the W_E. The relative importance of the inertial and viscous terms is sometimes expressed through the boundary layer Reynolds number,

$$Re \equiv \left(\frac{\delta_I}{\delta_M} \right)^3 .$$

Unlike α and δ_I, realistic magnitudes of the frictional parameters δ_M and δ_S are not known. Insofar as the solutions depend on parameters for which we have no reliable and independent estimate, the theory is not a deductive one—a concern raised by Ierley (1990) and also given considerable attention by Pedlosky (1996), hereafter P96. Furthermore, the form of the closures is dubious implying that "correct" values do not exist. Rigorous justification of subgrid parameterization exists only for the special case of a separation of length scales; i.e., a clear gap in the wavenumber spectrum. Unfortunately, recent satellite measurements suggest only a minor dip in the spectrum (Stammer, 1997). Furthermore, direct numerical simulations do not support the eddy viscosity hypothesis on which the lateral friction closure is based (see Lesieur (1997) and references therein).

However, if the solutions were not very sensitive to the true frictional terms, then rough parameterization may be adequate. That is, there may be a range of frictional parameters that give approximate representation to the frictional terms, and for which the large-scale solution remains reasonably constant. Unfortunately we do not know if this situation occurs, let alone for what parameter values. Intuitively one might expect insensitivity to small frictional parameters. One can partly justify using small A_H since it parameterizes the divergence of eddy fluxes of both QG and non-QG motions. In a numerical implementation, increasing grid resolution reduces the burden of parameterizing the former so eventually the non-QG parameterization should dominate. It is hoped that this occurs before the resolved motion becomes nongeostrophic (e.g., has large Rossby number, Ro). It is in this range of presumably small A_H that we hope that the QG solution both remains self consistent ($Ro \ll 1$) and becomes insensitive to subgrid scale parameterizations. The

alternative is that improved parameterization of subgrid scale processes or more sophisticated models are necessary even for a rough picture of the large-scale dynamics.

This paper addresses the possibility of insensitivity to A_H for solutions to the constant depth nonlinear Stommel-Munk model. The next section reviews some important background to this problem. In Section 3 we describe the requirements of a small Rossby number solution in the limit $max\,(\delta_M, \delta_S) \ll \delta_I \ll 1$. In Section 5, we present some numerical calculations based on the method described in Section 4. The focus of the numerical calculations is on steady solutions of the nonlinear Munk problem. The robustness of these results to the addition of Stommel friction, time dependence, change of boundary conditions and strength of forcing is considered.

2. Background

The ideal situation, as expressed by Pedlosky in P96, would be one in which the solution does not depend upon the poorly known frictional parameters and the related boundary conditions. For a wind-driven gyre with interior circulation that obeys the Sverdrup relation, this requires a boundary layer that feeds smoothly into the Sverdrup interior for all reasonable values of δ_M and δ_S. The problem is expressed in the general context of convergence of turbulence models in an article by Ierley and Sheremet (1995), hereafter IS95. The idea invoked is that of a turbulent cascade down to a viscous scale, with the large-scale flow becoming asymptotically independent of the viscosity. If this occurs, the model has *converged,* whereas *inertial runaway* is the scenario in which the large-scale flow increases without bound with increasing *Re*. Ierley and Sheremet focus on the nonlinear Munk model, though the issue applies to all OGCMs due to the necessity of subgrid scale parameterization.

Several studies have examined the behavior of the nonlinear Stommel and/or Munk model with $max\,(\delta_M, \delta_S) < \delta_I$: Veronis (1966), Böning (1986), IS95, Moro (1988), see P96 for a review. It is well established that for the single-gyre nonlinear Munk and Stommel models, the viscous-inertial boundary layer feeding into a Sverdrup interior gives way to inertial runaway as the dissipation is reduced. The small viscosity properties of the double gyre are less established. However, most studies suggest that the solution remains sensitive to the frictional parameters over the range studied, see for example Böning's runs of a nonlinear Munk model up to maximum $Re \approx 0.7$ (Böning, 1986), Le Provost and Verron's extensive parameter study using a model with Stommel type bottom friction and biharmonic lateral viscosity (Le Provost and Verron, 1987), and Moro's steady solutions to the nonlinear Munk problem using a nonsymmetric, double gyre forcing up to $Re \approx 5$ (Moro, 1988).

The inertial runaway phenomenon has been explained via the integral constraints on vorticity (P96, IS95) and kinetic energy (Cessi *et al.,* 1990). Integrating the vorticity equation over the area of the basin leads to the circulation equation. Note that for the single gyre problem, the wind-stress curl is of a single sign. Assuming a Sverdrup interior, scaling

arguments reveal (see P96) that the $O(1)$ input of vorticity cannot be balanced by bottom friction, nor by lateral friction in the limit of $max\,(\delta_M, \delta_S) \ll \delta_I$, when the free slip boundary condition is used. With the nonlinear Munk model and no slip conditions, an $O(1)$ flux of vorticity out of the basin occurs for the viscous sublayer on the western boundary. Since this contains only a fraction of the total transport, a steady solution cannot be found with Sverdrup interior. Numerical experiments of the time dependent case, where eddy fluxes of vorticity may transport vorticity to the sublayer, were carried out by Pedlosky, Ierley, and Young. The complete results were not published in journal article form, but are briefly described in IS95 and P96. They were discouraged to find inertial runaway with increasing *Re*.

The antisymmetric forcing of the double gyre problem has zero net vorticity forcing, but the above argument still applies for steady solutions that are symmetric about the gyre center latitude. One can show that the problem reduces to considering two single gyres with a free slip boundary condition along the latitude line of separation. However, advection of vorticity between regions of positive and negative vorticity forcing reduces the vorticity budget constraints. This may occur for both steady, nonsymmetric solutions as well as time dependent solutions, as discussed in Section 3.

Recently nonsymmetric, steady state, multiple equilibria for the double-gyre problem have been found by Jiang *et al.* (1995) in the shallow water context and Cessi and Ierley (1995), hereafter CI95, in the QG context. For nonsymmetric steady solutions (or in general for time dependent solutions) there may be an advective flux of vorticity between the north and south gyres, so the global vorticity budget imposes a weaker constraint. Because the problem cannot be considered as two single gyres separated by a zero vorticity line, the above arguments of P96 do not apply. In the case of the antisymmetric, double gyre forcing there is a net zero vorticity forcing term, and the global vorticity budget places no *a priori* restriction on the time dependent or nonsymmetric flows. Harrison and Holland (1981) and Marshall (1984) have shown that in a time dependent model, the eddy exchange of vorticity between the subtropical and subpolar gyres can be significant, which may delay the onset of inertial runaway. Primeau (1998) has found that the advection of vorticity in nonsymmetric steady solutions has an analogous effect with the eddy vorticity exchange. The nonsymmetric solutions of his double gyre model with biharmonic viscosity were found to delay the onset of inertial runaway. These solutions, even when linearly unstable, gave transports that more closely matched the time mean transport of some time dependent runs than the corresponding antisymmetric solutions at the same parameter values. However, the nonsymmetric solutions were found not to exist beyond a critical value of δ_I. This raises the question as to whether the nonsymmetric solutions exist in the parameter range of realistic δ_I and small frictional parameters. Limits imposed by finite grid resolution restricted us from establishing a definitive answer though we found they extend to at least $Re \sim 10$.

A net zero vorticity forcing is clearly a special case and requires some justification. The double gyre forcing, although still an idealization, is much closer than the single gyre

forcing to the observed wind-stress pattern over, for instance, the North Atlantic. Placing a solid boundary between the subtropical and subpolar gyres in the ideal models has been justified on the basis of the Sverdrup relation and the implied vanishing meridional velocity at the latitude of zero wind stress curl. In the nonlinear problem, however, this is no longer justified, as pointed out by Veronis (1966). Furthermore, for the world ocean the effect of vorticity cancellation may be even more important due to exchange between the two hemispheres. The robustness of the results to changes in the wind stress symmetry was addressed by also applying a nonsymmetric forcing for which there was a net vorticity input.

Consideration of the energy equation can also explain the inertial runaway problem. As pointed out by Cessi *et al.* (1990), for a Sverdrup interior the rate of energy transfer from the wind to the geostrophic flow, hereafter called the wind power input, P, remains $O(1)$ and is independent of the viscosity. In the nonlinear Munk problem the rate of kinetic energy dissipation by lateral friction, in both the inertial boundary layer and the viscous sublayer, becomes small with decreasing A_H, and thus precludes a solution in the limit $A_H \to 0$. This consideration is more general than that of the vorticity budget in the sense that it applies to both the transient and the steady cases.[3] It is easy to see that the same problem arises for the Stommel model, where the rate of energy dissipation term is rE, where E is the total kinetic energy. (This is discussed more fully in Section 3.) Holland (1978) argued that this is the relevant energy dissipation mechanism. Due to the inverse cascade of QG turbulence theory, little energy should be transferred to small scales, and hence lateral friction should dissipate little kinetic energy. He showed that transient eddies may transfer the kinetic energy to the bottom layer where it is dissipated by (length scale independent) bottom friction. This however, requires large values of r that may not be realistic. Small values of r are not compatible with a Sverdrup interior (see Section 3).

Allowing for a non-Sverdrup interior may also alleviate the constraints of the energy budget. Consider the QG energy equation for general boundary conditions,[4]

$$\frac{dE}{dt} = -\iint \psi \frac{W_E}{f_0 H}\, dx\, dy - Diss \tag{3}$$

where the area integral is over the entire domain. The first term on the RHS is P. Note that for a non-Sverdrup interior, P is a function of the solution. This alleviates the constraint of an $O(1)$ energy source term, as the solution may "shut off" the source term. The last term on the RHS is the rate of dissipation of kinetic energy, and is discussed further in Section 3. There it is shown that for Ro to remain small in the limit of small frictional parameters, P must be less than for a Sverdrup interior. This shutting off of P may affect the small δ_M properties; if the source term becomes smaller, the problem of inertial runaway may be delayed.

3. However, aspects of the solution must be assumed, such as the Sverdrup interior.
4. The constant ρH has been factored out for simplicity.

As the frictional parameters are reduced the flow generally becomes unstable, and the relationship between the steady state solutions and the time mean flow is not well established. We note that there is some evidence that aspects of the unstable solutions may be related to the time mean behavior, for example Legras and Ghil (1985), Primeau (1998), and Primeau (personal communication). Although these issues are beyond the scope of the present paper, the robustness of the main results was addressed by comparison with the time dependent solutions. An eigenanalysis may also provide interesting information, (see for example, Sheremet *et al.* (1997)); however, it is beyond the scope of the present paper. The analysis of the numerical solutions is herein focused on the integral properties, which it is hoped reveal some important aspects of the QG dynamics.

3. Requirements of small Rossby number solutions for small frictional parameters

Although there are at least two ways to derive the nonlinear Stommel and Munk models, the QG approximation is a standard approach. We consider the energy budget of the nonlinear Stommel-Munk problem to deduce the restrictions on P for solutions that are consistent with the small Rossby number of the QG approximation. We focus on the limit where $max\,(\delta_M, \delta_S) \ll \delta_I \ll 1$. It is found that P must be much less than that for the Sverdrup solution. This result depends upon the assumption that the maximum velocity occurs at the inertial length scale or less, the inertial length scale being estimated by $\delta_I L_x$. With $\delta_I \approx 0.025$ and $L_x \approx 4000$ km, the inertial length scale estimate is 100 km. This is comparable to the width of the western boundary current and the length scale of mesoscale eddies, which observations support as having greater velocities than the larger-scale flow. This assumption excludes the 'basin filling gyre solutions' from consideration. Otherwise the consideration is general. We avoid the problem of specifying where significant dissipation occurs by considering the extreme limit of maximum dissipation throughout the domain. As such, this is not an estimate of realistic dissipation, but an upper bound which nonetheless leads to the surprising restrictions on P. We also consider realistic basin dimensions with $\alpha = O(1)$.

For the QG system to be valid we require both the maximum Rossby number, Ro, and planetary number, R_p, to be small. They are defined as,

$$Ro \equiv \frac{U}{f_o L}, \qquad R_p \equiv \frac{\beta L_y}{f_o} = \tan(\phi)\frac{L_y}{a}, \tag{4}$$

where U is a velocity scale, f_o is the Coriolis parameter at the basin center latitude ϕ, L is a flow length scale and a is the radius of the earth. For a midlatitude ocean $\tan(\phi) \approx 1$ and the basin may extend at least half the radius of the earth, so $R_p \approx (L_y/\alpha) \approx 0.5$. Although formally the small R_p assumption is tenuous, the results below are not sensitive to this; e.g., the power input to the planetary geostrophic and quasi-geostrophic Sverdrup interior are similar. A minimum requirement is that $Ro \leq R_p$. The more severe restriction of $Ro < 0.1$ will also be addressed.

Consider the QG energy equation, (3), for the nonlinear Stommel-Munk problem with

general boundary conditions. In a steady state or statistical equilibrium, an energy balance requires P to be balanced by the rate of dissipation, *Diss.* The latter has three terms: one for dissipation by lateral friction in the interior, one for interior dissipation by bottom friction, and a final term representing the flux of kinetic energy through the boundaries, giving

$$Diss = 2A_H Z + 2rE - A_H \oint \mathbf{u} \cdot \hat{\mathbf{t}}\zeta \, dl,$$

where the line integral is around the perimeter of the basin and Z is the total enstrophy

$$Z \equiv \tfrac{1}{2} \int\int \zeta^2 \, dx \, dy.$$

Recall that the boundary term is zero for no slip or free slip boundary conditions. An upper bound for each term is found below.

The vorticity scales like (Rof_o), so that

$$2A_H Z \leq A_H (Rof_o L_x)^2 \alpha. \tag{5}$$

Since Ro is bounded for valid QG solutions, this upper bound on dissipation by lateral friction decreases with A_H. In order to find an upper bound on E that is consistent with small Ro, we need a length scale for the maximum velocity, u_{max}. As stated above we use $\delta_I L_x$. This gives $u_{max} \leq (\delta_I f_o L_x Ro)$ so that,

$$rE \leq \frac{r}{2} (\delta_I f_o Ro)^2 \alpha L_x^4. \tag{6}$$

Thus, as for lateral friction, a bounded Ro implies that the upper bound on dissipation by bottom friction decreases with r. Using the same assumption of the length scale $\delta_I L_x$ for u_{max}, we can write the upper bound on the boundary term as,

$$A_H \oint \mathbf{u} \cdot \hat{\mathbf{t}}\zeta \, dl \leq A_H \delta_I L_x (f_o Ro)^2 2(L_x + L_y) \tag{7}$$

$$\leq 4A_H (f_o L_x Ro)^2 \delta_I \alpha, \tag{8}$$

where the assumption of $\alpha \geq 1$ has been used. Note that the boundary term is $4\delta_I$ relative to the lateral friction term, as revealed by dividing (8) by (5). Since $\delta_I \ll 1$ the boundary term can be dropped.

Combining these results reveals that for bounded Ro, the upper bound on the total rate of dissipation decreases with the frictional parameters A_H and r. For a steady state or statistical equilibrium in the limit where A_H and r approach zero, this implies that either P must approach zero or the small Rossby number approximation (and hence QG) must break down. But this is an extreme limit; also of interest is the intermediate range of frictional parameters. To see what restrictions on P apply in this parameter range, it is helpful to normalize the equations so the notion of 'small' frictional parameters will have more meaning.

A useful reference for normalizing the energy equation is provided by the standard view

of a Sverdrup interior and narrow western boundary current. Here the power input from a zonal wind stress is predominantly in the interior, and the energy source term can be approximated as,

$$P \approx P_{Sv} = -\iint \psi_{Sv} f_o W_E H^{-1}\, dx\, dy. \tag{9}$$

The argument could be developed for arbitrary W_E, however to do so would result in introducing a nonstandard δ_I below. To avoid this we proceed by taking W_E to be a function of y alone. A Fourier series decomposition gives,

$$W_E(y) = a_0 + \sum_{n=1}^{\infty} a_n \sin\left(n\pi \frac{y}{L_y}\right). \tag{10}$$

For the case where $a_0 = 0$ one can easily show that,

$$P_{Sv} = \frac{\alpha L_x^3}{4\beta}\left(\frac{f_o W}{H}\right)^2. \tag{11}$$

Note that the ideal single and double gyres problems are just the special cases of retaining only the terms $n = 1$ and $n = 2$ in (10), respectively.

Combining the above results, (5) and (6), and dividing by (11), the QG steady state energy equation gives,

$$\frac{P}{P_{Sv}} \le \frac{4}{\delta_I}\left(\frac{\alpha Ro}{R_p}\right)^2\left[\frac{1}{Re} + \frac{\delta_S}{\delta_I}\right]. \tag{12}$$

In the limit of $max\,(\delta_M, \delta_S) \ll \delta_I \ll 1$, the term in square brackets will be much less than one. However, the behavior of the RHS is complicated by the factor multiplying the square bracket term. The situation can be made more concrete by substituting values for the observable parameters. Starting with the (more certain) geometrical parameters, we have for a typical basin, $\alpha = O(1)$, $R_p = O(0.5)$. In the Gulf Stream one may encounter $Ro = O(0.1)$. A reasonable δ_I is in the range $0.01 < \delta_I < 0.04$, so we suggest $\delta_I = 0.025$ as typical. (Although we have set $\delta_I = 0.025$, we retain δ_I within the square brackets for comparison with frictional parameters.) This leads to,

$$\frac{P}{P_{Sv}} \le O\left(\frac{6}{Re} + \frac{6\delta_S}{\delta_I}\right). \tag{13}$$

Thus, using observed values for parameters, we find that $P < P_{Sv}$ for a surprisingly large range of frictional parameters: $Re > 6$ and $6\delta_S < \delta_I$.

These arguments were motivated by the issue of insensitivity to subgrid scale parameterization of the constant depth nonlinear Stommel-Munk model in the limit $max\,(\delta_M, \delta_S) \ll \delta_I \ll 1$. Clearly (13) implies that a Sverdrup interior solution is not valid in this limit. This was obtained using observed δ_I and Ro, but is still an extreme upper bound in the sense that

it was derived for the case of *significant dissipation via mesoscale eddies throughout the basin.* In a realistic flow the dissipation will be less than that allowed for above. This means the restrictions on P for small Ro solutions are likely stronger than given by (13).

Taking the Sverdrup balance as a valid description of the interior, one may interpret the above argument slightly differently. Returning to (12), the LHS is then one and the inequality represents a restriction on the range of frictional parameters consistent with a Sverdrup interior. Recall that the Sverdrup balance involves assuming that, for $\alpha = O(1)$,

$$\delta_I^2 \ll 1$$
$$\delta_M^3 \ll 1$$
$$\delta_S \ll 1.$$

Combining these constraints with (12), again using $R_p = O(0.5)$ and $Ro = O(0.1)$, one obtains a window on the acceptable range of frictional parameters. For the nonlinear Munk model,

$$6\delta_I^4 \leq \delta_M^3 \ll 1. \tag{14}$$

For the Stommel model,

$$6\delta_I^2 \leq \delta_S \ll 1. \tag{15}$$

Because we considered the extreme case of significant dissipation throughout the domain, the LHS inequalities represent extreme lower limits on the frictional parameters. As mentioned above, in a realistic flow the dissipation will be less. Under the present interpretation, this means that the lower limits on δ_M and δ_S are likely larger than given by (14) and (15). In other words, a Sverdrup interior is consistent with small Ro for only a *very narrow range* of frictional parameters.

Allowing for a non-Sverdrup interior, we regain the possibility of small Ro solutions in the limit $max\ (\delta_M, \delta_S) \ll \delta_I \ll 1$, but only if P can drop below that of the Sverdrup interior case. But nothing has suggested that actual solutions will shut off P. This must be tested numerically. Below we describe the model equations and the method of solution. The results are presented in Section 5.

4. Model descriptions

a. *Steady-state model*

For an idealized double-gyre, the Ekman pumping velocity is often represented by

$$W_E = -W \sin(2\pi y/L_y). \tag{16}$$

Assuming this form of W_E, the steady state version of (1) in nondimensional form is,

$$\alpha^{-3}\delta_I^2 J'(\psi', \nabla'^2\psi') + \psi'_{x'} = -\sin(2\pi y') + \alpha^{-4}\delta_M^3 \nabla'^4\psi' - \alpha^{-2}\delta_S \nabla'^2\psi' \tag{17}$$

where primed variables are dimensionless. The independent variables are scaled by the basin dimensions, $(x, y) = (L_x x', L_y y')$, and the streamfunction scale is obtained via a Sverdrup balance,

$$\Psi \equiv \frac{f_o W L_x}{\beta H}. \tag{18}$$

The dimensionless Laplacian operator is defined as

$$\nabla'^2 \equiv \left(\alpha^2 \frac{\partial^2}{\partial x'^2} + \frac{\partial^2}{\partial y'^2} \right).$$

Two boundary conditions were specified on all boundaries. Setting $\psi' = 0$ at the boundary resulted in the no normal flow, kinematic, boundary condition. Additionally, the dynamic boundary condition was specified as either no slip ($\psi'_{n'} = 0$, where n' is the normal direction) or free slip ($\nabla'^2 \psi' = 0$).

The other nondimentional variables follow from the definitions above. For example, the nondimensional total kinetic energy is defined as,

$$E' \equiv \tfrac{1}{2} \iint (\psi'_{x'})^2 + \alpha^{-2} (\psi'_{y'})^2 \, dx' dy', \tag{19}$$

where the area integral is over the entire basin. Similarly, P' is defined as,

$$P' \equiv \iint \psi' \sin(2\pi y') \, dx' dy'. \tag{20}$$

Primes will be dropped from the nondimensional variables where there is no danger of ambiguity. Note that for a Sverdrup interior, we have $P_{Sv} = 0.25$.

Following CI95, we solved (17) on a rectangular domain with $\alpha = 2$. Whereas they used Chebyshev polynomials, we obtained the ψ field on a uniform grid of N interior points. The PDE was transformed to a system of N nonlinear algebraic equations with derivatives approximated by centered differences, and the Jacobian term was discretized according to the energy and enstrophy conserving scheme of Arakawa (1966). For a given set of parameters, the system was solved using a Newton-Raphson algorithm. The solutions were followed through parameter space using a pseudo-arclength continuation algorithm (see, e.g., Seydel, 1994). The most computationally expensive step involved solving an N^{th} order linear system at each iteration of the Newton-Raphson method. The matrix was sparse and banded so an LU decomposition algorithm was used to solve the linear system. The computational cost increases strongly with N and this effectively limited the obtainable resolution. Most calculations were performed with $N = 175^2$ which required approximately 260MB of RAM. Several solutions per hour could be found on a Silicon Graphics Incorporated POWER CHALLENGE XL R8000. Using interative methods for solving the linear system greatly reduces the memory requirements. Several methods were attempted, including the conjugate gradient routine SPARSE.F provided by Numerical Recipes (Press *et al.,* 1986), the biconjugate gradient method, LINBCG.F (Press *et al.,*

Table 1. Summary of steady state numerical runs.

Run	δ_I	δ_M	δ_S	α	γ	Boundary conditions	min δ_v
1	0.025	0.0112 − 0.060	0	2	0	free slip	0.0075
2	0.04	0.0127 − 0.044	0	2	0	free slip	0.0072
3	0.025	0.0129 − 0.037	0	2	0	no slip	0.0093
4	0.025	0.0098 − 0.031	0.012	2	0	free slip	0.0061
5	0.025	0.0111 − 0.157	0	2	0.25	free slip	0.0074
6	0.025	0.0101 − 0.024	0	2	−0.25	free slip	0.0064

1992), and the Lanczos method, implemented in the NAG Mark 15 library. However, these were found to increase the execution time to impractical lengths. This may be due to the Jacobian matrix becoming almost singular. Preconditioning might help, but this avenue was not explored. Few continuation codes use interative linear solvers; an exception is described by Dijkstra *et al.* (1995).

The smallest length scales of a solution must be well resolved for the algebraic system to correspond to the PDE. We consider the effects of finite resolution in two ways. First we estimate the smallest length scale as the viscous sublayer width, obtained via a balance between the advection and diffusion of relative vorticity (e.g., Pedlosky, 1987),

$$\delta_v = \sqrt{\frac{\delta_M^3}{\delta_I}}.$$

A minimum requirement is to have the grid spacing less than δ_v, i.e. $175^{-1} \approx 0.0057 < \delta_v$. The minimum δ_v for each run is listed in Table 1, revealing that there was at least one grid point in the viscous sublayer (not counting the boundary point) for all calculations. The accuracy of the numerical results was also assessed by comparison with those obtained with different resolutions, as described in Section 5b.

b. Time dependent model

For the time dependent simulations, we must add the Eulerian time derivative term to (17), giving

$$\alpha^{-2}\nabla^2\psi_t + \alpha^{-3}\delta_I^2 J(\psi, \nabla^2\psi) = -\psi_x - \sin(2\pi y) + \alpha^{-4}\delta_M^3\nabla^4\psi - \alpha^{-2}\delta_S\nabla^2\psi. \quad (21)$$

The time scale, $T_o \equiv (L_x\beta)^{-1}$, is of the order of 10 hours. This equation was solved numerically using the same spatial descritization described above, and a semi-implicit, trapezoidal rule time stepping for the nonlinear terms (Arakawa and Lamb, 1977). That is, at each time step we must solve for the vorticity, ζ^{n+1}, such that,

$$(\zeta^{n+1} - \zeta^n)\Delta t^{-1} + 0.5\alpha^{-1}\delta_I^2(J(\psi^n, \zeta^n) + J(\psi^{n+1}, \zeta^{n+1})) = \mathrm{RHS}^n \quad (22)$$

where n, $n + 1$ refer to the past and present time steps and RHS is the right-hand side of (21). This nonlinear equation was solved by iteration. The Poisson equation $\nabla^2\psi = \alpha^2\zeta$ was solved using the very efficient multigrid algorithm of the NAG Mark 15 library.

The choice of time step was based upon satisfying the Courant-Friedrichs-Lewy criterion with the maximum velocity estimated as δ_I^{-1}. Courant number 0.2 allowed for rapid convergence in most simulations.

While the semi-implicit time stepping employed here is more expensive than say leap frog or Euler's method, it was chosen for its conservation properties. A trial simulation was performed with only the nonlinear terms; i.e., RHS $= 0$ in (22); the energy and enstrophy were both conserved to better than 0.25 parts per thousand for 10,000 time steps. The grid resolution was limited by computation time (not memory requirements). For the 321×321 grid used it took about an hour for 600 time steps on the Silicon Graphics Incorporated POWER CHALLENGE XL R8000.

5. Results

The main purpose of this section is to describe the results of the energetics analysis in relation to the analysis of Section 3. First, however, we briefly describe the experiments performed, the types of solutions found and properties of the bifurcation curves.

a. Experiments

Solutions of (17) were traced through parameter space using the model described above. While CI95 kept the eddy viscosity parameter fixed and increased the wind strength parameter, we kept the wind forcing constant, and decreased the eddy viscosity. While both result in a higher Re, an important difference was noted by IS95. For the former, a structural adjustment (that of $\nabla^2\psi$ becoming a tighter function of ψ) can take place to satisfy the vorticity equation without increasing ψ. For the latter, this is not the case, and they suggest that this explains their observation that ψ increased globally, without bound, as A_H was decreased. It is common practice to investigate high Re behavior by using larger δ_I as opposed to smaller δ_M; the latter is more computationally demanding. Because we were motivated by the issue of insensitivity to subgrid scale parameterization it was necessary to use a realistic range of δ_I, based upon observations, and vary the frictional parameters.

The steady state experiments are summarized in Table 1. For the base case (run 1), we used $\delta_S = 0$, free slip boundary conditions, and $\delta_I = 0.025$. Variations about the base case were performed (runs 2 to 6) to test the robustness of the results. For a comparison with the time dependent behavior we performed the simulations summarized in Table 2. For all numerical experiments $\alpha = 2$.

For run 2, we increased δ_I to represent a strong wind forcing case. The choices of δ_I can be related to observable properties. Recall that Ekman theory gives W_E in terms of the

Table 2. Summary of time dependent simulations.

Simulation	δ_I	Re	δ_S	α	γ	Boundary conditions	Initial solution
1	0.025	4	0	2	0	free slip	A1
2	0.025	4	0	2	0	free slip	N1
3	0.025	4	0	2	0	free slip	mean of 2

surface wind stress, so we can write,

$$\delta_I = \left(\frac{2\pi\tau_o}{\rho H \beta^2 L_x^3} \right)^{1/2},$$

where τ_o is the magnitude of the wind stress. With $H = 1000$ m to represent the upper ocean, and on a midlatitude β-plane of zonal extent $L_x = 2000$ km, a typical wind stress of $\tau_o = 0.3$ Pa gives $\delta_I \approx 0.025$. To represent the strong forcing case, we used $\delta_I = 0.04$ in run 2, which corresponds to $\tau_o \approx 0.8$ Pa. Note that for larger scale systems, e.g., $L_x = 4000$ km and for the total barotropic flow $H = 5000$ m, $\delta_I = 0.04$ corresponds to a very strong wind field, and as such can be considered an upper bound on the realistic δ_I for large scale, midlatitude basins. A useful chart relating values of δ_I to various values of L_x and H can be found in Le Provost and Verron (1987). It would be preferable to investigate smaller values of δ_I but this would limit the accessible range of Re.

To test the robustness of the results to the symmetry of the wind stress, we performed runs 5 and 6 with nonsymmetric wind stress. The forcing term had the form,

$$W_E = -(1 - \gamma(y' - 0.5))W \sin(2\pi y'). \tag{23}$$

Note that for $\gamma = 0$ the forcing term of (17) is recovered. However, for $\gamma \neq 0$ the forcing term is no longer antisymmetric in y, and there is a net vorticity forcing.

We performed time dependent simulations at $Re = 4$ and other settings corresponding to run 1. The simulations differed only in the initial solutions, see Table 2.

b. *Steady state solutions and bifurcation curves*

Only three of CI95's solutions have order Sverdrup interior velocities, the antisymmetric, A1, and the pair of nonsymmetric solutions, N1; the others are basin filling gyres and can be rejected as unphysical.[5] These solutions, found using the model described above, are plotted for reference in Figure 1. Similar solutions were found with no slip boundary conditions. At higher Re the N1 solutions developed small length scales through stationary eddies and waves, see Figure 2. As pointed out by CI95, (1) satisfies the symmetry

$$\psi \to -\psi, \qquad y \to -y, \tag{24}$$

5. The current speed may be of the order of 50 m/s, thus exceeding the wind speed. In such a situation, the wind stress depends upon the current, which is not accounted for by the model.

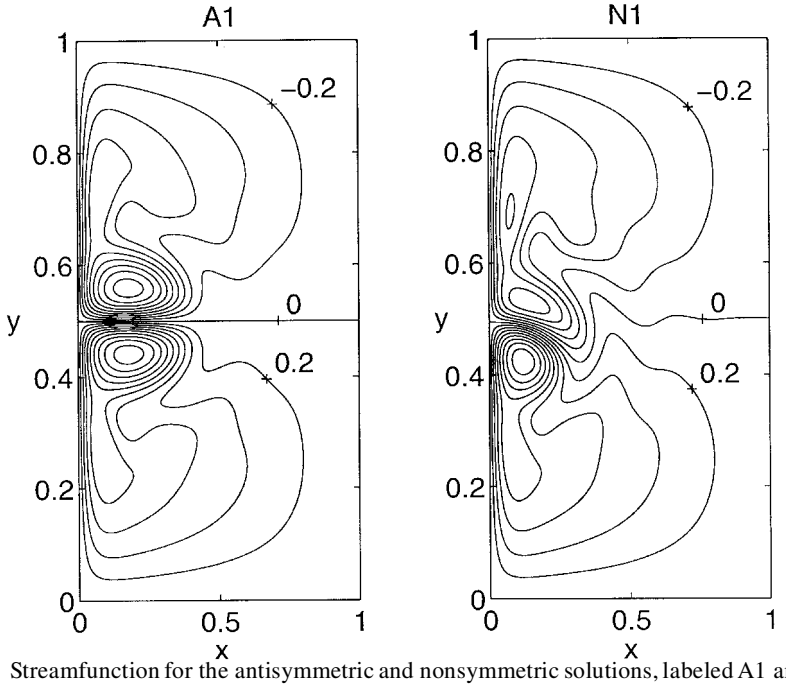

Figure 1. Streamfunction for the antisymmetric and nonsymmetric solutions, labeled A1 and N1 in CI95. Here $\delta_M = 0.03$, and the other settings correspond to the base case (run 1): free slip boundary conditions, $\delta_I = 0.025$, $\delta_S = 0$, $\gamma = 0$ and $\alpha = 2$.

when,

$$W_E(x, y) = -W_E(x, -y).$$

Hence the nonsymmetric solutions are in fact pairs of solutions, related by (24). Note that for $\gamma \neq 0$, this symmetry relation in no longer valid.

A bifurcation curve for the base case is shown in Figure 3. Here we plot ψ_{max} versus Re. We see the familiar pitchfork bifurcation giving rise to the N1 solution type, consistent with CI95 and Primeau (1998). Two stationary bifurcations were found along the A1 solution branch, presumably giving rise to the N2 and N3 branches (Primeau, 1998). No stationary bifurcations were found along the N1 branch; however, we did not test for Hopf bifurcations. Some studies have used different names for the solution branches on different sides of a turning point. This is impractical in the present context and is not adopted; 'N1', for instance, will herein refer to the complete branch unless otherwise stated.

High values of Re led to numerical problems. Using the 175×175 grid we found an increasing density of turning points that eventually led to a complicated, 'spaghetti' like structure in the region of $8 < Re < 11$, Figure 4. Comparison with the results obtained with finer grids (275×275 and 218×436) provided an indication of the sensitivity to resolution and range of validity of the results. In Figure 4 the course resolution bifurcation curve is seen to shadow the high resolution curve up to about $Re \approx 7$, after which they

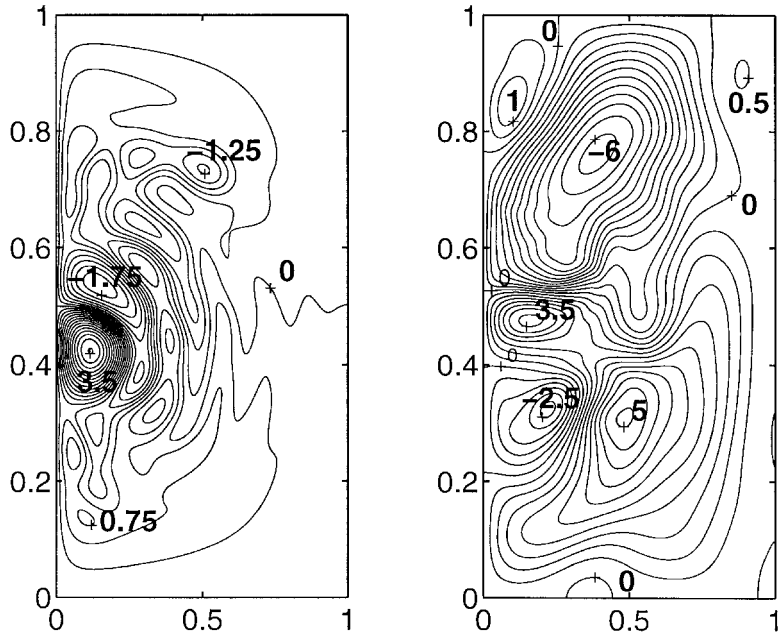

Figure 2. Sample streamfunction fields for the nonsymmetric solutions. Left: steady state solution. Right: instantaneous time dependent solution 2000 time units after initializing the model with the time mean solution of simulation 2. For both fields $\delta_M = 0.01575$ ($Re = 4$) and the other settings correspond to the base case (run 1).

diverge rapidly. Clearly the lower resolution results are affected by the numerical discretization and cannot be trusted beyond $Re = 7$. At $Re = 8$ the relative vorticity fields had developed jagged oscillations at the grid spacing in the narrow region along the midlatitude jet. The streamfunction appeared deceptively smooth; however, the second order derivatives associated with the Laplacian operator revealed the numerical problems. These results highlight the difficulty in obtaining reliable solutions at low A_H. For the 175×175 grid ($\Delta x \approx 0.0057$) there were almost three points in the Munk layer ($\delta_M = 0.013$) and almost two points in the viscous sublayer ($\delta_v \approx 0.0095$). It appears that the nonlinear terms can give rise to very small length scales in the interior that lead to numerical problems.

The validity of the solutions with fine resolution grids can be assessed by a comparison of 275×275 and 218×436 grid results. The latter had much more resolution in the y-direction to help resolve the jet region where fluid parcels of extreme difference in vorticity come together. This curve seems to follow the 275×275 grid results though they may be departing round $Re \simeq 11$. By this point the viscous sublayer is not well resolved for the 218×436 grid and the jet region is not well resolved in the 275×275 grid. Clearly a nonuniform grid focusing more resolution in these two trouble areas would be advantageous.

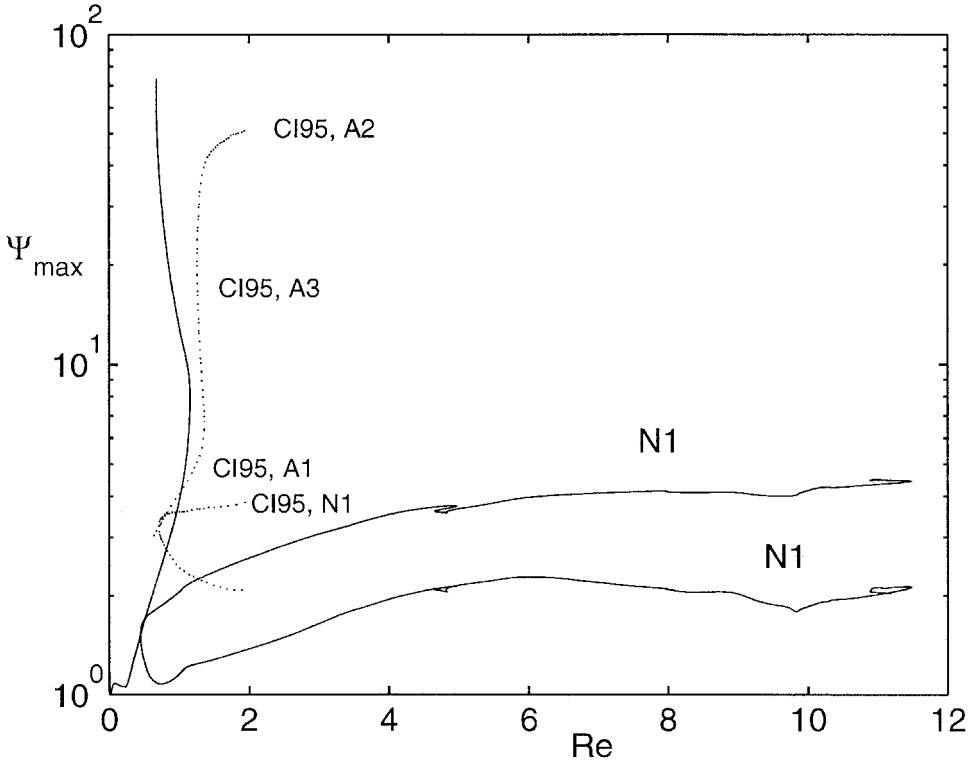

Figure 3. Bifurcation diagram ψ_{max} vs. *Re* for the base case (run 1): free slip boundary conditions, $\delta_I = 0.025, \delta_S = 0, \gamma = 0$, and $\alpha = 2$. A pitchfork bifurcation leads to the pair of N1 solutions. Also shown are the A1, A2, A3, and N1 branches of CI95.[6] Two other stationary bifurcations (not shown) were found along the A1 branch at $Re \approx 8.5, 11$, presumably indicating the origin of the N2 and N3 branches. The upper curve labeled N1 corresponds to the maximum streamfunction that can be seen in Figure 1 occurring in the strong inertial recirculation in the subtropical gyre. The solution corresponding to the lower curve labeled N1 is the mirror image partner of the solution in Figure 1.

Despite the differences revealed in Figure 4 between the high and low resolution grids beyond $Re \simeq 7$, the streamfunction fields looked quite similar. For the integral quantities, *P*, *E*, etc., the discrepancy was quite small for all values of *Re*. However, as the robustness calculations (runs 2 through 6) used the 175 × 175 grid, we suggest these bifurcation curves should be interpreted with caution, especially with regard to the location of turning points, beyond $Re \simeq 7$.

6. CI95 is for $\delta_M = 0.0478$. Our results for that case (not shown) were visually indistinguishable from their results, except for a factor of 2. our program gave ψ_{max} approaching 1.17 for small δ_I, consistent with Pedlosky (1987, p. 282 (5.4.48)).

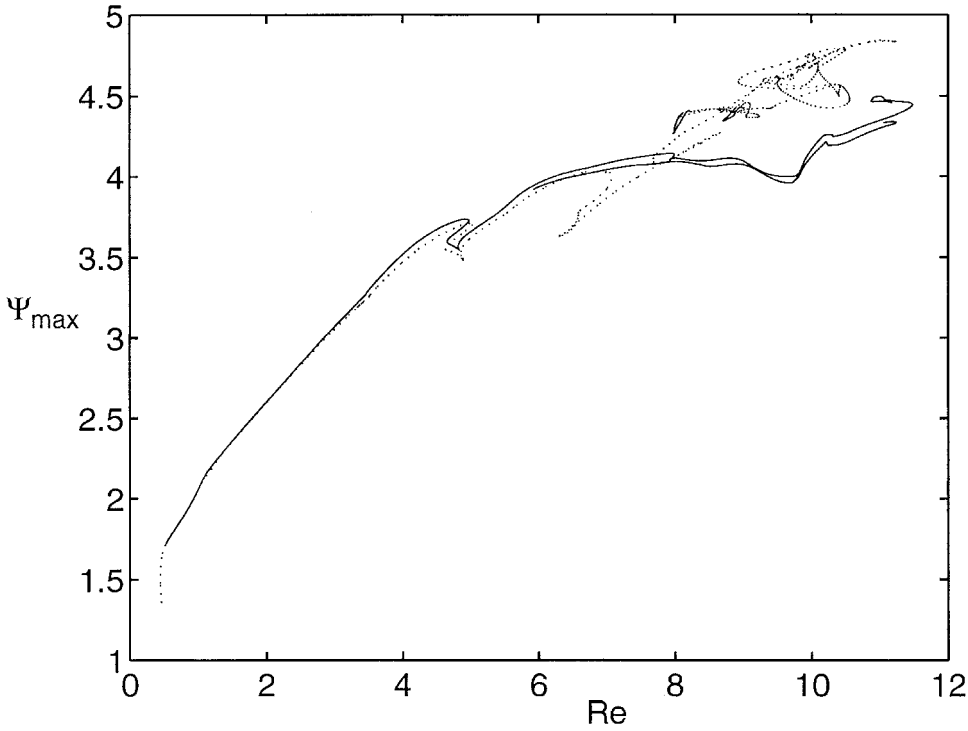

Figure 4. Bifurcation diagram for the base case (run 1), ψ_{max} vs. *Re*. The dotted line represents the data obtained with a 175 × 175 grid, the long solid line a 275 × 275 grid, and the short solid line a 218 × 436 grid (more points in the *y*-dir).

Recall that previous studies, CI95 and Primeau (1998), have found that the N1 solution ceases to exist for δ_I greater than a critical value. There a single 'fold catastrophe,' or turning point, connects the N1 and N2 solution branches. Unfortunately the case of increasing *Re* by holding δ_I at a realistic value and decreasing δ_M appears more difficult to compute. We stopped computing the bifurcation branch because we cannot trust the solution beyond where it becomes sensitive to the discretization. We cannot state definitely whether or not the N1 solutions cease to exist for δ_M less than a critical value; however, we have confirmed that they extend to the range of fairly small δ_M, $Re \sim 10$.

A similar bifurcation structure was found for the strong forcing case (run 2). In Figure 5 we have focused on just the nonsymmetric solutions, plotting $\psi_{max} + \psi_{min}$ which is zero for the A1 solutions. Some of the turning points appeared as sharp kinks that might suggest the continuation algorithm has jumped branches. This necessitated reproducing the curve with smaller step length and magnifying the plot around the suspicious areas—a smooth curve gave us more confidence that only one branch was being followed. Note that this is different from showing that the solutions are not spurious, which requires showing that they are not sensitive to *grid spacing* as opposed to pseudo-arclength *step length.*

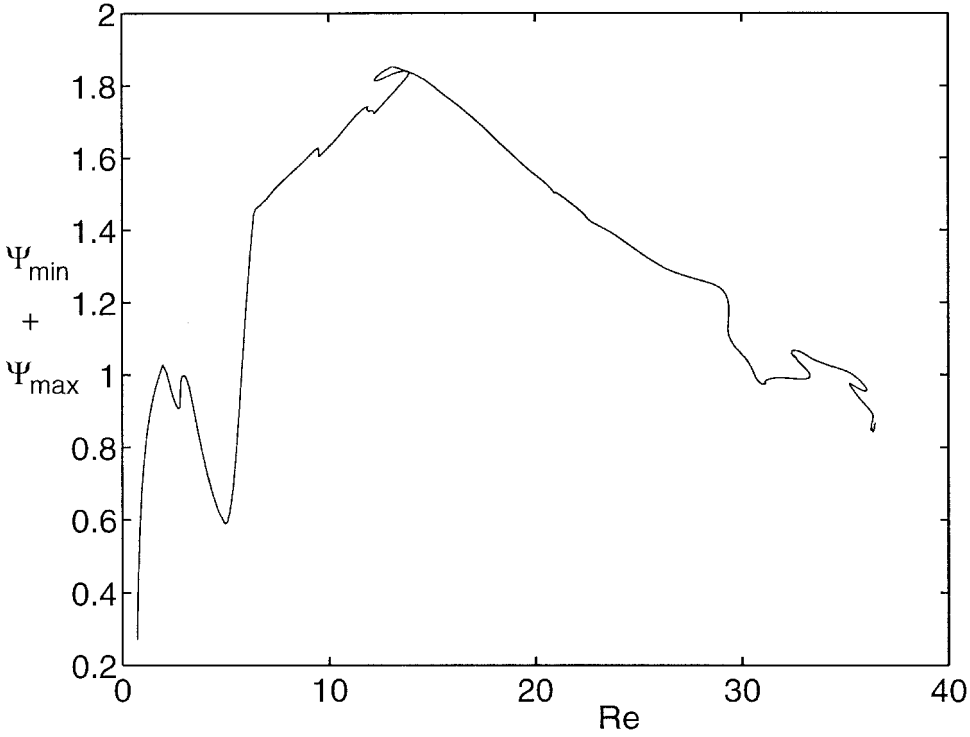

Figure 5. $\psi_{max} + \psi_{min}$ vs. *Re* for run 2, displaying the N1 solutions. The redundant portion of the curve, obtainable via the transformation (24), has been omitted.

c. Time dependent simulations

Because the steady state solutions become unstable for increasing *Re* we performed three time dependent simulations with fixed parameters corresponding to the base case with $Re = 4$; i.e., $\delta_M \simeq 0.01575$. Complete analysis of these solutions is beyond the scope of the present paper; here we focus on the relation of the statistics of the energetics to that of the steady state solutions.

The solutions were obtained using the model described in Section 4b. There was no available A1 solution at $Re = 4$ so we initialized the first simulation with an A1 inertial runaway solution obtained with lower *Re*, while keeping *Re* in this simulation fixed at $Re = 4$. For the second simulation the model was initialized with the corresponding N1 steady state solution with $Re = 4$. While it would be interesting to go to higher *Re*, we found that very high resolution was required to obtain a smooth vorticity field, especially in the region of the midlatitude jet. At $Re = 4$ we found that a grid of 321×321 interior points was required.

To obtain stationary statistics we had to spin up the model to a statistical equilibrium state. For practical reasons, the notion of stationary statistics is not treated rigorously. The choice of spin up time was based upon inspection of the history of the kinetic energy time

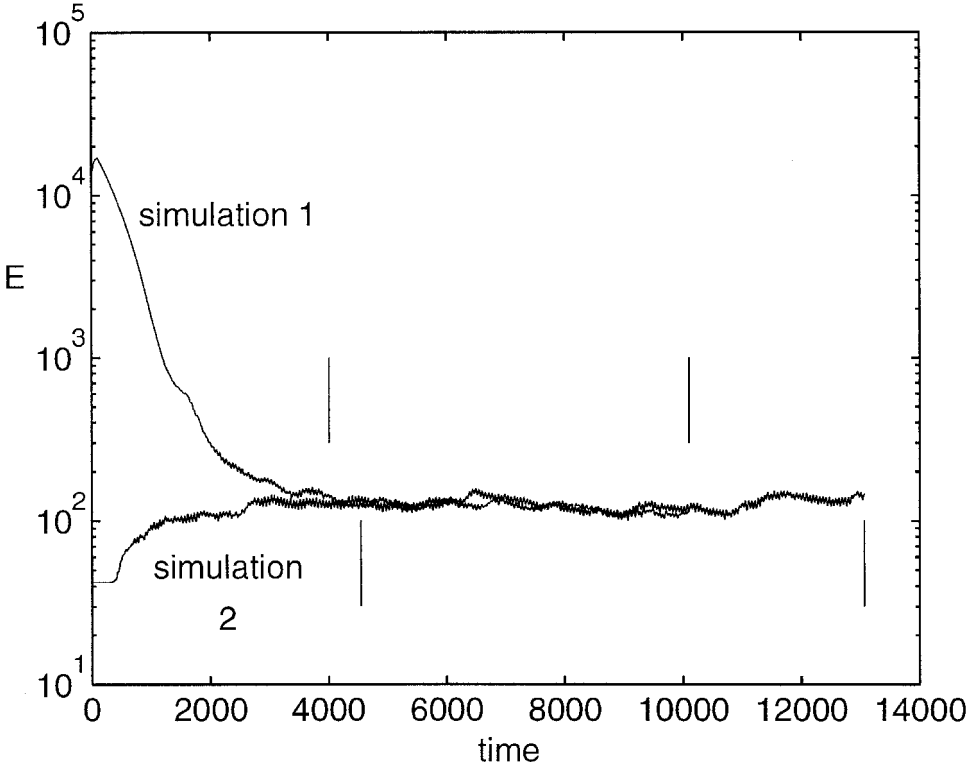

Figure 6. E vs t: Parameters are given in Table 2. Simulation 1 (2) was initialized with an A1 (N1) solution. The upper (lower) pair of vertical lines indicates the period over which simulation 1 (2) was averaged to obtain the statistical parameters.

series, see Figure 6, and can be estimated as $t' = 3750$ (150,000 time steps). However, there appears to be several interacting oscillations of different periods including "interannual variability." Furthermore, the time series of other diagnostics, not shown due to lack of space, revealed interesting statistical variations after the spin up period, suggesting a multimodal behavior. This is consistent with the simulations done by McCalpin and Haidvogel (1996). While longer time series would be required to characterize this variability, it seems likely that the simulations performed here are adequate to estimate the means of the various diagnostics considered.

The fields were then averaged every time step from $t' = 4037$ to 10162 (steps 161,500 to 406,500) for simulation 1 and from $t' = 4578$ to 13140 (steps 183,125 to 525,625) for simulation 2. These averaging periods represent several weeks of computation time and were partly chosen for practical reasons. The mean streamfunction fields are compared in Figure 7. The mean solutions bare a close resemblance and appear to have "forgotten" their different initial conditions. Further statistics of the simulations are discussed below for which the averaging periods are always as stated above.

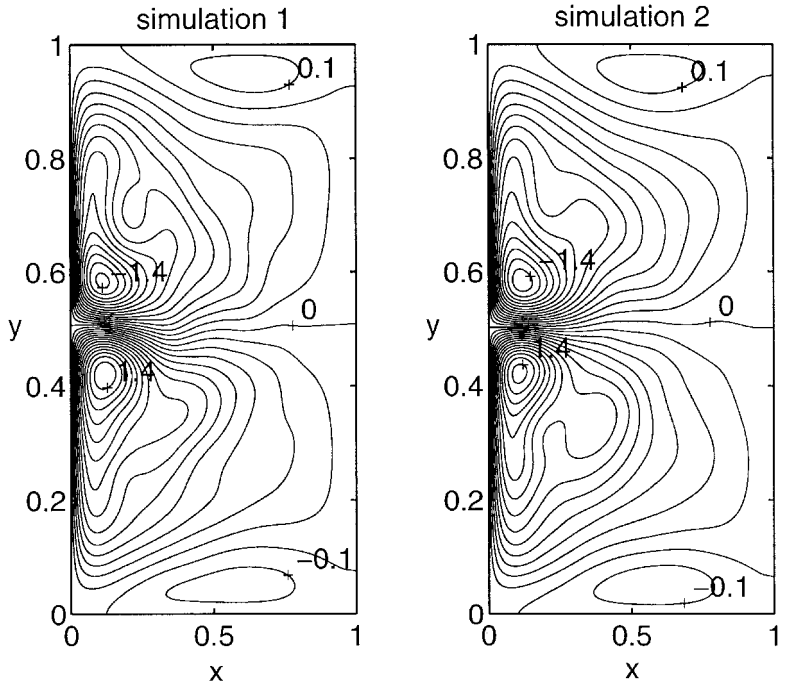

Figure 7. Time mean streamfunctions for the simulations 1 and 2, refer to Figure 6 for details. The similarity between the two fields supports the claim that the solutions have "forgotten" the initial conditions.

The third simulation was initialized with the time averaged streamfunction field and integrating for 2000 time units. This filtered out the greatest basin modes (Sheremet *et al.,* 1995). An instantaneous solution is compared with the N1 steady state solution at the same parameters in Figure 2.

d. Analysis of solutions

i. Wind power input. Here we consider the behavior of P defined in (20), and compare it with $P_{Sv}(=0.25)$ as discussed in Section 3. The dependence of P on Re was very different for the antisymmetric and nonsymmetric solutions. P is plotted vs. Re in Figure 8 for the base case. We first describe this case and then consider the robustness with respect to changes in δ_I, δ_S, γ, and dynamic boundary condition. The time mean of the time dependent simulations were also compared to the steady solution results.

For the antisymmetric solutions P increased rapidly with Re for $Re > 1$. The opposite occurred for the nonsymmetric solutions; P for the N1 solutions generally decreased with increasing Re. For $Re > 1$, P for A1 solutions was much greater than for N1 solutions. This observation may allow for a simple physical explanation. If we write the QG energy equation in terms of the surface wind stress, τ, the source term is expressed as the rate at

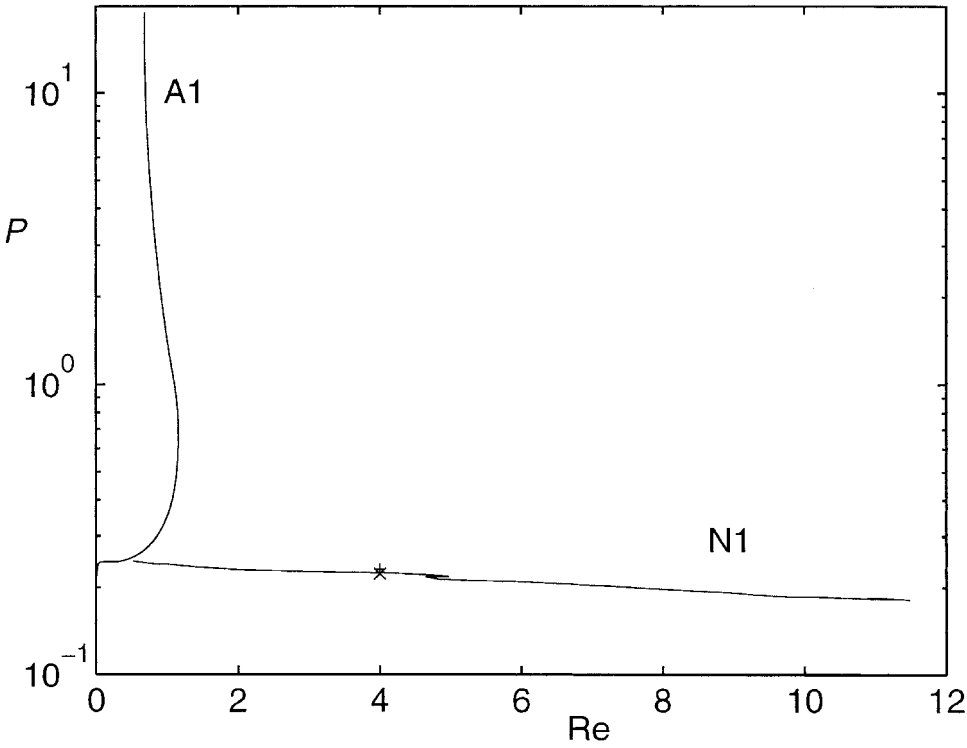

Figure 8. P vs. Re for the base case (run 1). The shutting-off of P for the N1 solution is contrasted with the rapid increase for the A1 solution. The first and second time dependent simulations, shown as 'x' and '+', agree to within 4% of each other and are almost indistinguishable from the steady state N1 branch.

which the wind does work on the geostrophic flow,

$$P = \int\int \mathbf{u} \cdot \tau \, dx \, dy,$$

where again the area integral is over the basin. This expression has the form of a covariance between $\mathbf{u}$ and τ. The interpretation is that a higher correlation between the velocity and stress fields corresponds to a higher P. (Of course, velocities of higher magnitude also increase P.) The Ekman pumping field used here corresponds to a stress field of $\tau^s = -\cos(2\pi y)$, which is symmetric about its maximum at $y = 0.5$. The A1 solutions have a $\mathbf{u}$ field symmetric in y, which is better able to correlate with the symmetric τ. More specifically, the energetics may have been dominated by the influence of the strong eastward midlatitude jet, which for the antisymmetric solutions was directly in line with the maximum wind stress. The nonsymmetric solution achieved lower P by deflecting the jet away from the gyre center.

Consider the magnitude of P in Figure 8. For $Re < 1$ the A1 solution resembled the Sverdrup solution, so we expect $P \approx P_{Sv} = 0.25$. However it was slightly less than one

quarter due to the effect of finite boundary layer width. For the N1 solution type, P dropped below one quarter for the range of Re investigated. This trend started well before $Re > 6$ where the restrictions discussed in Section 3 implied that either P would start to decrease or the small Rossby number assumption would be violated. The numerical results for the nonsymmetric solutions are consistent with the restrictions of (13) since it was derived as an extreme upper bound with significant dissipation throughout the domain. However, this must be interpreted in conjunction with the Ro behavior, as considered in Section 5d(*ii*).

The robustness of these results was considered by changing the values of δ_I, δ_S, γ, changing to no slip boundary conditions and comparison with the time dependent simulations. As discussed in Section 5c, the two time dependent simulations appeared to forget their initial conditions and approached the same statistical state. Not surprisingly then the time mean P of both simulations agreed very closely (to within about 4%) and are barely distinguishable in Figure 8. Furthermore, their values straddle P for the N1 steady solutions. This demonstrates that the shutting off of P can also occur in the full time dependent equations.

The time series of P showed oscillations on many time scales, the shortest of which was approximately 31 time units (about 13 days) with a smooth curve of peak to peak amplitude of about 2. This is much larger than the mean $P \sim 0.23$ and suggests that positive and negative exchanges of energy between the currents and the "atmosphere" dominate viscous dissipation on these time scales. This is consistent with the findings of Sheremet *et al.* (1995) in the context of the time dependent single gyre problem with no slip boundary conditions. An analogous phenomenon has also been found for the real ocean (Scott, 1999). There we used TOPEX/Poseidon data to calculate P to the North Pacific and found complex oscillations about the mean with peak to peak amplitude approximately equal to the mean.

For the strong forcing case (run 2, $\delta_I = 0.04$) P vs. Re is plotted in Figure 9. Here the behavior for the N1 and A1 solutions was qualitatively similar to the base case, with a rapid increase in P for the A1 solution as Re was increased above one. The N1 solutions again tended to decrease P for increasing Re. For run 2 a higher Re was obtainable so the arguments of Section 3 are more applicable; the N1 solution reached $Re > 30$. Since P was significantly less than one quarter the solution was shutting-off the power input well below that of the Sverdrup solution. However, Ro was increasing with Re, as discussed below.

Although the base case and the strong forcing cases gave similar quantitative results, some quantitative differences were noted. Plotting together the A1 solutions from the two runs (not shown) we found that the P curve is shifted toward higher Re in the strong forcing case. This suggests that some of the details may be lost when unreasonably high δ_I are used to obtain high Re. However, the general trend of P shutting off with Re for the nonsymmetric solutions seems robust to changes in δ_I.

In run 3 no slip boundary conditions were used. Some qualitative differences in P vs. Re were found, see Figure 9. The most obvious difference is that $Re = 1$ no longer marks the point where P for A1 started increasing rapidly with increasing Re. This point has been

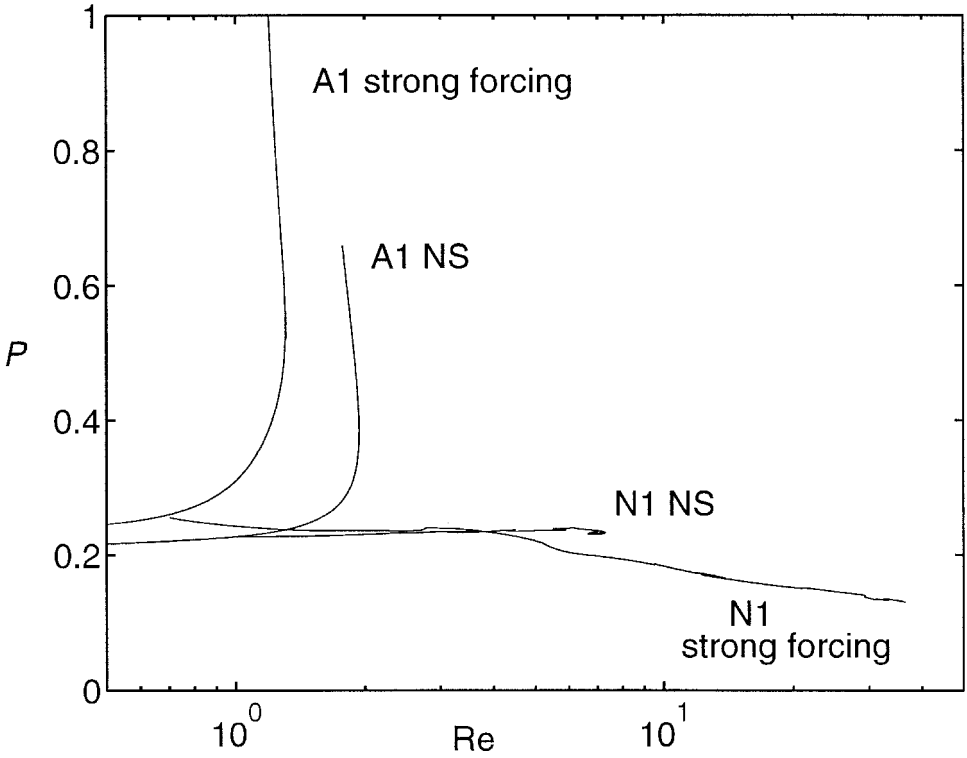

Figure 9. P vs. Re for the strong forcing $\delta_I = 0.04$ (run 2) and no slip boundary conditions (run 3). Other parameters are as in run 1.

shifted toward higher Re in the no slip case probably due to the viscous damping of the solution by the no slip boundary layer. This is consistent with the result found by Sheremet *et al.* (1997); for the nonlinear Munk single gyre problem, they compared the position of the cusp point for no slip and free slip solid boundaries. For the no slip case, the cusp point is shifted toward higher Re. A second qualitative difference was found; P for the N1 solution no longer decreased with increasing Re, but actually increased slightly. However, the sharp contrast between the A1 and N1 solutions, as observed for the free slip base case, appeared robust to changes in boundary condition. As we see in the next subsection, the no slip case also had much higher Ro.

In run 4 bottom friction was added with $\delta_S = 0.012$ (for which $\delta_M = \delta_S$ at $Re \approx 9$), see Figure 10. First we describe some of the differences in the bifurcation structure for this run. The spaghetti structure does not appear. At the highest Re only one closed eddy appeared in the streamfunction field. The N1 branch goes through a single turning point at $Re \approx 11.5$ and rejoins the A1 branch. The N2 solution was easily identified as the upper branch that leads back to the A1 branch.

Regarding P for run 4 we see the qualitative separation between the antisymmetric and

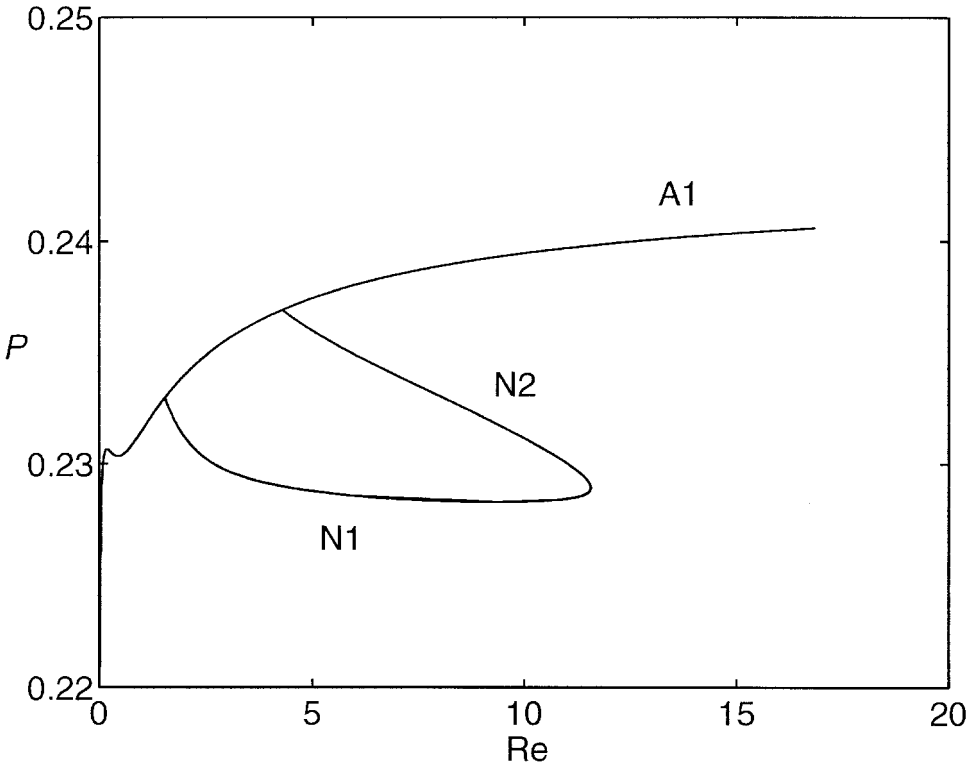

Figure 10. P vs. Re for the bottom friction case (run 4): $\delta_S = 0.012$, other parameters are as in run 1. The N2 solution branch starts with a pitchfork bifurcation from the A1 solution branch and joins the N1 branch at the turning point.

nonsymmetric solution types. The qualitative results discussed for the base case remain: P for A1 solutions increased with Re, while the opposite occurred for the nonsymmetric solutions. For the N1 branch, P decreased with Re until near the turning point. For the N2 branch, P was monotonically decreasing with Re. However, for the A1 solutions, P was here concave downward. That is, at higher Re, P for the A1 solutions increased more slowly with increasing Re. The curve tends to level off with increasing Re, as expected. For $Re > 9$, $\delta_S > \delta_M$ and we expect the solution to be less sensitive to changes in δ_M.

For runs 5 and 6 the nonsymmetric forcing term was used via the introduction of the new parameter γ defined in (23). For positive γ the Ekman pumping is stronger in the subtropical gyre, a significant feature of the Northern Hemisphere wind field. For small γ the behavior can be anticipated with bifurcation theory. The pitchfork bifurcation is a nongeneric feature when only one parameter is varied. Recall that here (and elsewhere, e.g. CI95) the pitchfork bifurcation was found at various pairs of δ_M and δ_I. The dilemma is resolved by the existence of symmetry properties of the governing equation; here we have the QG symmetry described in (24). In group theory, the equation is said to satisfy the

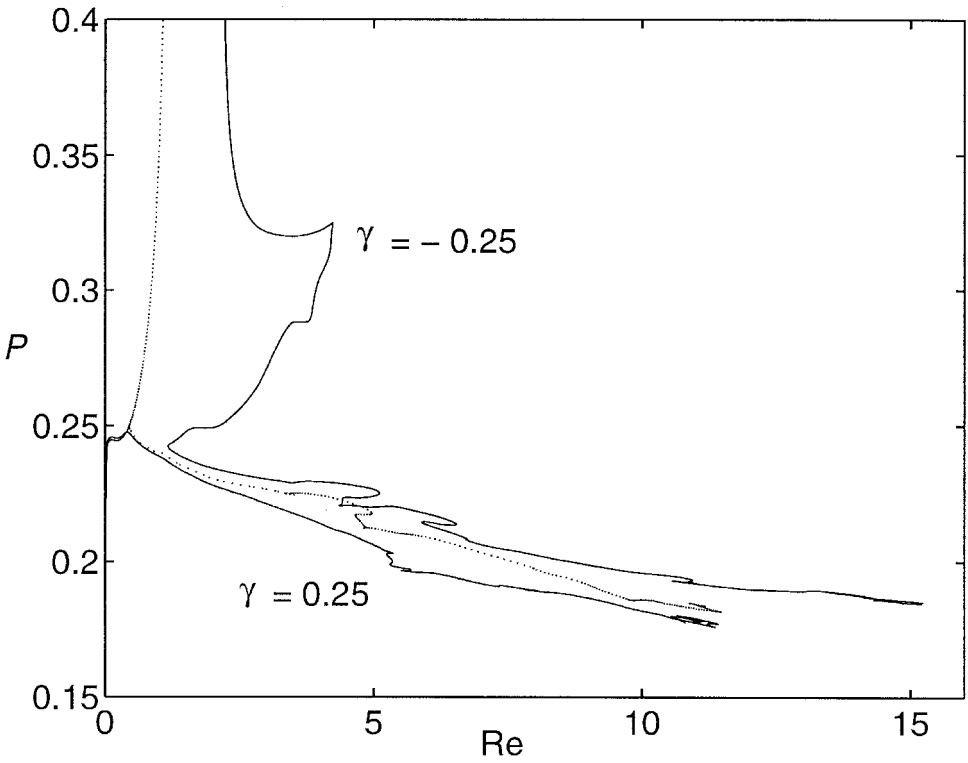

Figure 11. *P* vs. *Re* for the nonsymmetric wind stress (runs 5 and 6): $\gamma = \pm 0.25$, other parameters are as in run 1. The dotted lines are from Figure 8 for reference.

cyclic group of order two equivariance, refer to Seydel (1994, p. 105). It is well known that the pitchfork bifurcation is generic for equations satisfying this equivariance, but that it is structurally unstable. That is, arbitrary perturbations remove the equivariance and the pitchfork bifurcation is lost. Here for $\gamma \neq 0$ the symmetry relation is broken and this must destroy the pitchfork bifurcation for our system to remain generic. However, the solution branches cannot completely disappear, since the implicit function theorem requires that for small changes in a parameter, the regular equilibrium solutions[7] must remain nearby. Thus a small change $\gamma = 0 \rightarrow \gamma = \varepsilon$ should open the two solution curves (intersecting at the pitchfork bifurcation) to two neighboring nonintersecting curves.

For finite γ the behavior cannot easily be anticipated and we must perform the numerical experiments. Hence γ was varied continuously to $\gamma = 0.25$, then held fixed while δ_M was varied for run 5. Because the QG symmetry is broken this should be done for both of the antisymmetric pairs of the N1 solutions. However, one can easily show that it is equivalent to use only one of the N1 solutions but take $\gamma = -0.25$ as well. This was done for run 6. The results for *P* are compared with run 1 in Figure 11. The $\gamma = 0.25$ curve follows very

7. Regular solutions can be parameterized such that the Jacobian is not singular.

closely, though is everywhere slightly below, the N1 curve from the base case. The $\gamma = -0.25$ shows two distinct regimes. The lower branch also follows very closely, though is almost everywhere slightly above, the N1 curve from the base case. The upper branch has completely different behavior, which resembles somewhat the A1 branch from run 1. The main result then is not overly sensitive to the symmetry properties of the wind field.

ii. The small Rossby number approximation. Consider whether the solutions found here are consistent with the QG approximation of $Ro \ll 1$. The maximum Rossby number may be estimated as $Ro = (U_{sv}/L_x f_o)$ max (ζ'). Using the definition of R_p, we have,

$$Ro = \frac{\delta_I^2 R_p}{\alpha^3} max\,(\nabla'^2\psi'). \tag{25}$$

We calculated Ro based on (25) with $R_p = 0.5$. It was found that Ro depended most strongly upon Re, boundary conditions and solution type.

The most striking contrast was between the nonsymmetric solutions with no slip and free slip boundary conditions. Ro vs. Re for runs 1 and 3 is plotted in Figure 12 to highlight the effect of dynamic boundary condition. For the free slip solutions, the requirement of small Ro was never grossly violated while Ro quickly became greater than one for the no slip solutions. Recall that for free slip boundary conditions, one can scale the vorticity in the inertial boundary layer as $L\beta$, where L is the meridional extend of the displacement of a fluid particle. Normalizing this by f_o we find $Ro = O(R_p)$. For the free slip N1 solution, Ro appears gradually to approach R_p for increasing Re. The strong forcing case looked similar (not shown), where Ro reached 0.4 at $Re = 35$. For no slip boundary conditions one expects maximum vorticity in the viscous sublayer and, as pointed out by a reviewer, the standard scaling gives, $\zeta_v = O(U_{sv}/\delta_v\delta_I)$ and thus $Ro = R_p\sqrt{Re}$. Hence it is not surprising that Ro increased more rapidly with Re in the no slip case. But it is clear from Figure 12 that the no slip scaling is only applicable at lower Re; increasing Re resulted in Ro significantly larger than predicted by scaling. The strong recirculation at higher Re causes the larger velocity in the inertial boundary layer and hence greater vorticity.

The location of the maximum vorticity revealed no surprises. For the no slip case the maximum vorticity occurred along the western boundary layer. For the free slip condition, the vorticity is forced to zero along the boundaries. The location of the maximum was more scattered, but mostly occurred around the strong recirculation.

For the time dependent simulations we have calculated the time mean of the Rossby number; this is plotted in Figure 12 as a '+'. Also plotted are the maximum and minimum of Ro, 'x', giving an indication of the variability. (For simulations 1 and 2 these quantities agreed to within 1%, so only one set of results is plotted.) The mean Ro does not differ significantly from the steady N1 solution result at $Re = 4$. Even the maximum Ro is much less than the no slip scaling and the N1 no slip curve. We also calculated Ro for the time mean streamfunctions; the two simulations gave results differing by about 6%, however for

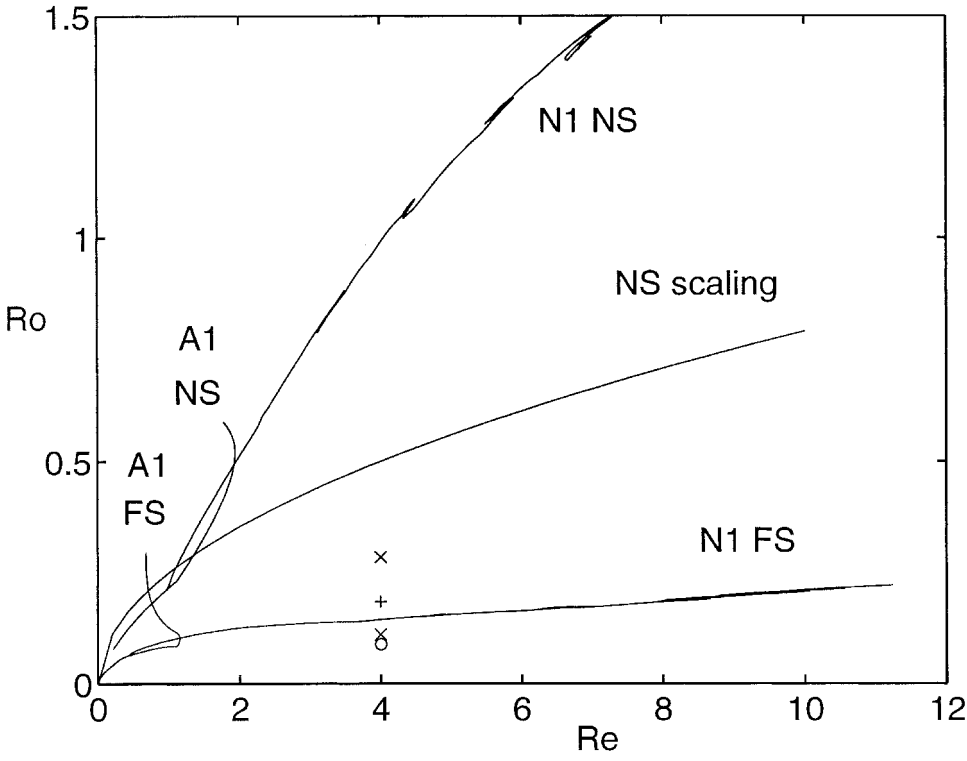

Figure 12. *Ro* vs. *Re* for free slip (run 1), no slip (run 3) and time dependent simulations. The line labeled "NS scaling" allows a comparison to the theoretical no slip result. The two simulations agreed to within 1% so only one result is plotted. The mean (*Ro*) is shown as '+' along with the max (*Ro*) and min (*Ro*), 'x'.

clarity only the result for the second simulation is shown (as an 'o'). This was less than the minimum *Ro* due to the smoothness of the time average streamfunction field.

It is perhaps worth emphasizing that the solutions for which $Ro > 1$ are no longer valid QG solutions on a large, midlatitude β-plane. This reveals an important difference between the two dynamic boundary conditions. Recall that, as discussed in Section 1, scaling arguments give that for no slip boundary conditions, the viscous sublayer is able to remove $O(1)$ vorticity. The results here suggest that the cost is a violation of the small *Ro* approximation used to justify the QG model. In Section 3 we were left with the result that in the limit $max\ (\delta_M, \delta_S) \ll \delta_I \ll 1$ either *P* shuts off or *Ro* becomes large. For the N1 no slip solutions, it appears that both may occur. The situation for free slip is less clear.

The *Ro* dependence on *Re* for the antisymmetric solutions was different. The A1 solutions followed closely the N1 solutions until a critical *Re*, after which *Ro* increased almost vertically. For free slip this occurred at $Re \approx 1.15$ where the A1 solution branch goes through a turning point (after which it is called the A3 solution) analogous to that found by Cessi and Ierley, (see Fig. 6 in CI95). The transport of the solution also increased

rapidly as the solution developed toward a basin filling gyre mode, called A2 in CI95. As mentioned earlier these are clearly unphysical, and the branch was not followed to higher *Re*. These solutions have maximum velocities at large length scales (not δ_I) so the assumptions discussed in Section 3 do not apply.

iii. Internal compensation via advection of vorticity. In the introduction it was suggested that the nonsymmetric solutions may allow for advection of vorticity across the basin center latitude, as found by Primeau (1998), and analogous to the eddy fluxes discussed by Harrison and Holland (1981) and Marshall (1984). Integrating the advection term from (17) over the southern half of the basin and using the kinematic boundary condition, we obtain,

$$\int_0^{1/2}\int_0^1 \alpha^{-1}\delta_I^2 J(\psi,\zeta)\,dx\,dy = \alpha^{-1}\delta_I^2\int_0^1 \psi_x\zeta\,dx$$

where the integral in x is taken at $y = 0.5$. This is an advective flux of vorticity between subtropical and subpolar gyres. In order to address the significance of this, we normalized this quantity by the magnitude of vorticity forcing over the south half of the basin, giving

$$\frac{\pi\delta_I^2}{\alpha^3}\int_0^1 \psi_x\nabla^2\psi\,dx, \tag{26}$$

which we shall call normalized vorticity advection. It is plotted versus *Re* for the base case in Figure 13, revealing an increase with *Re*. At the highest values of *Re*, a significant portion of the vorticity input was advected across the basin center latitude. At $Re = 4$ the advection of vorticity by transient eddies (simulation 2) is only slightly higher than that by the stationary solutions. This important feature of the steady state solutions is restricted to the nonsymmetric solutions.

As discussed in Section 1 and P96 the intergyre advection of vorticity significantly reduces the burden on the boundary layers to diffuse vorticity out of the basin. However, the normalized vorticity advection was significantly less than one so that a considerable amount of vorticity was diffused through the walls. That is, the vorticity budget was not solely met by advection (which is a logical possibility for the special case of zero net vorticity forcing). This is in contrast to Primeau (1998) where no diffusion through the walls was ensured by the choice of boundary conditions. For the case of nonsymmetric winds there is a nonzero net vorticity forcing. Yet run 5 ($\gamma = 0.25$), shows very close agreement with the symmetric wind stress case. The results of run 6, not shown, were much more complicated. This is probably a result of the two qualitatively different regimens of run 6, as revealed in Figure 11.

iv. Kinetic energy. Analysis of the total kinetic energy, E defined in (19), revealed interesting differences between the energetics of the antisymmetric and nonsymmetric solution types. The magnitude of E also served as a proxy for inertial runaway. As pointed

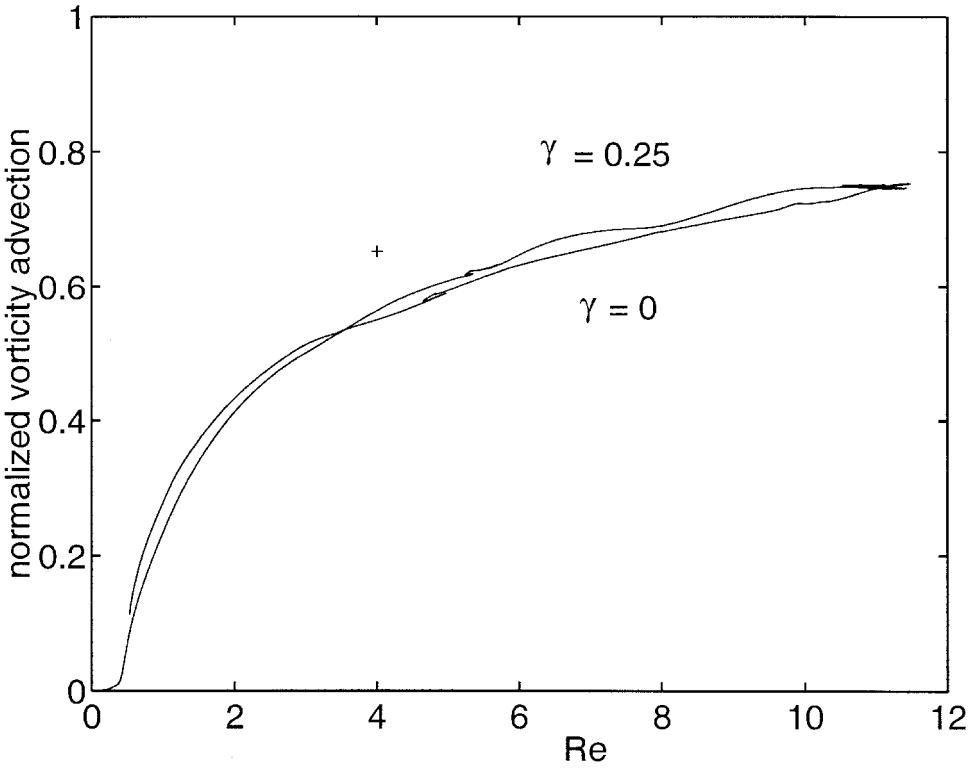

Figure 13. Normalized vorticity advection between gyres vs. *Re* for N1 solutions for run 1 ($\gamma = 0$), run 5 ($\gamma = 0.25$) and simulation 2 '+' ($\gamma = 0$ and $Re = 4$). Other parameters are as in run 1. The vorticity advection is normalized as in (26).

out by an anonymous reviewer, a useful reference point for E is the linear Munk solution total energy, which is approximated as the energy in the Munk boundary layer:

$$E_{Munk} = \begin{cases} (4\delta_M)^{-1} + O(1), & \text{free slip} \\ (8\delta_M)^{-1} + O(1), & \text{no slip.} \end{cases} \tag{27}$$

See Sheremet *et al.* (1995) for the derivation. For $Re \leq 0.25$ both the no slip and free slip steady solutions agreed closely with linear theory. However, for $Re > 1$, the nonlinear solutions have much larger E; free slip results are shown in Figure 14. In all cases E continued to increase as Re was increased. However for the nonsymmetric solutions the rate of increase in E with Re is tapering off at higher Re. This gives the intriguing suggestion that the total energy may become insensitive to the subgrid parameterization for the steady solutions as A_H becomes small. Recall that the maximum streamfunction also appeared insensitive to δ_M between approximately $5 < Re < 11$, see Figure 3. Note that this interpretation is somewhat exaggerated by the logarithmic scale on the vertical axis in both these figures.

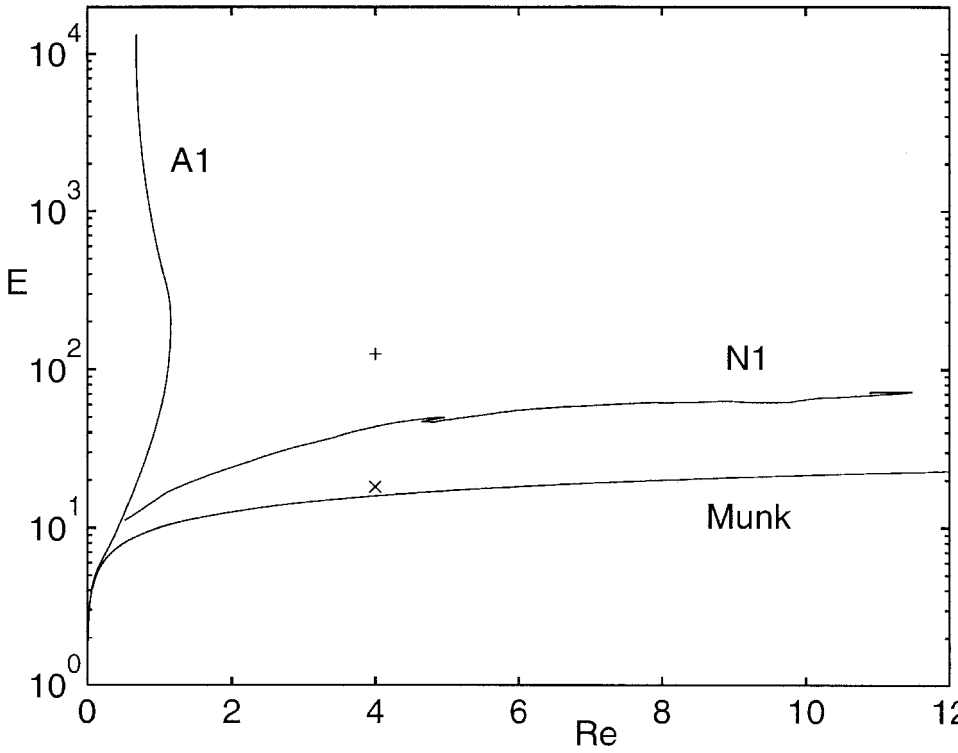

Figure 14. Total kinetic energy, E, vs. Re for the base case (run 1) and the time dependent simulations. The two simulations agreed to within 1% so only one result is plotted. The energy of the mean ψ field, 'x', is only 15% of the mean energy, '+', indicating that 85% of the energy is in the eddy field. The mean field energy is only about 12% higher than that given by the linear Munk solution.

Comparison of the antisymmetric and nonsymmetric solutions again reveals interesting differences. For all runs, E of the A1 solutions blew up for lower values of Re than for the corresponding nonsymmetric solutions. These results can be understood in terms of two effects. Visual comparison of the antisymmetric and nonsymmetric solutions suggests that the latter developed smaller length scales which aided dissipation. Also the nonsymmetric solutions can maintain global energy and vorticity budgets by partially shutting off P, and by advection of vorticity between regions of positive and negative forcing, as described earlier. As a result, for the narrow parameter range where both A1 and N1 solutions were found, the N1 solutions appear to be less sensitive to the value of Re, since the magnitude of the slope of E is less.

Recall that for the time dependent simulations the clear distinction between the antisymmetric and nonsymmetric solutions was lost as the simulations forgot their initial conditions. This raises the question of how the extremely large energy of the solution initialized with the A1 inertial runaway solution was removed? This occurred in simulation

1 during a rapid spin down period that started around $t' = 100$ and essentially finished by $t' = 1500$. Interestingly, frictional dissipation played only a minor role; a large and negative P, almost an order of magnitude larger than the dissipation, was the chief energy removing mechanism. This extreme example of shutting off P only lasted during the short spin down phase of simulation 1.

After the initial transient periods, the mean E of the two time dependent simulations agreed to within 1% and hence only one result is plotted in Figure 14. Approximately 85% of the energy is in the eddy field; the mean field contains only 15% of the energy. The latter is surprisingly close to the corresponding Munk solution which is consistent with Sheremet *et al.* (1995).

The time series of E showed oscillations on many time scales, the shortest of which was approximately 31 time units; this corresponds to the period found in the P time series discussed above. This mode was not present in simulation 3, which had the basin modes filtered by initializing the simulation with the time average solution. Instabilities then excited lower frequency modes. However the corresponding frequency was found in Kamenkovich *et al.* (1995) to be the predominant period of self sustained oscillations. (Their period was 125 time units; after accounting for a factor of $\alpha^2 = 4$ scaling the frequency when we write the basin mode equation, the equivalent of Eq. (16) in Kamenkovich *et al.* (1995), we then find that the frequencies are very close.) This suggests different modes of instability between the double and single gyre systems. Unfortunately lack of space must limit this comparison.

6. Discussion

a. Summary

We were motivated by an interest in a model that is not sensitive to poorly known parameterizations. The focus of this study was on the possibility of the QG model becoming independent of δ_M as Re was made large while keeping δ_I at realistically small values. Hence in Section 3 we related the limit of $max\,(\delta_M, \delta_S) \ll \delta_I \ll 1$ to the energetics. There, an upper bound of the kinetic energy dissipation rate was found using the small Ro approximation and assuming maximum velocities have inertial length scales or less. This was expressed as an upper bound on P in terms of standard nondimensional parameters and P for a Sverdrup interior flow. To obey the small Ro criterion, P must decrease with increasing Re and δ_I/δ_S. This was assessed numerically using the steady state nonsymmetric, N1, and antisymmetric, A1 solutions CI95.

In analyzing the energetics, the A1 and N1 solutions displayed interesting differences. For the range of parameters investigated where they coexist, P for the A1 solutions was greater than P for the N1 solutions. The qualitative behavior was solution-type dependent as well. For the A1 solutions types, P increased rapidly with increasing Re while for the nonsymmetric solution types P decreased slightly. These results were essentially robust to changes in δ_I, δ_S, dynamic boundary condition, and forcing sysmmetry. For no slip boundaries, P for the N1 solutions increased slightly with Re. With the addition of bottom

friction the increase in P with Re for the A1 solutions occurred less rapidly for $\delta_S > \delta_M$ as expected. The numerical calculations indicate that, for high enough Re, the restrictions on P were apparent, but for the N1 solutions only.

The observed differences in P between the nonsymmetric and antisymmetric solutions was explained physically. The hypothesized mechanism was the decorrelation between the wind stress and geostrophic current for the N1 solutions causing lower P. The antisymmetric solutions on the other hand, had a very strong midlatitude jet directly in line with the maximum wind stress, producing a very strong P. This appeared to dominate the energetics and is consistent with the corresponding difference in E.

Metaphorically speaking, the multiple equilibria provide the steady system with a choice on how to maintain the energy balance. The system can select the symmetric solution with large P, and hence requires large velocity gradients to dissipate the energy flux. Alternatively the system can select a nonsymmetric solution with lower P, requiring lower dissipation rates.

The time dependent simulations initialized with the A1 and N1 solutions revealed that both steady solutions were dynamically unstable at $Re = 4$. The simulations seemed to forget their initial conditions and approach a similar statistically steady regime. The time average behavior of all quantities considered was much closer to the steady N1 solutions than to the A1 inertial runaway solutions; P agreed within about 3% with the steady N1 solutions. Comparing the time series of P and viscous dissipation, we found that the positive and negative exchanges of energy between the "atmosphere" and "ocean" were dominant over viscous dissipation for short time scales.

The possibility of maintaining an energy balance via selecting a low P is intriguing, and may have analogies in other areas of physics. The central force problem provides a familiar though incomplete analogy. For kinetic energy less than potential energy, periodic solutions are possible in the ideal system. Without dissipation the total energy is conserved and the orbit must be such that the rate of energy transfer to an orbiting mass is zero. Examples of systems with small P can be found in fluid mechanics as well. For inertial oscillations in an approximately steady and uniform wind field, the wind energy input over one half period will tend to cancel the input of the other half period. Hence, P will be a minimum.

While the A1 solution was strongly dependent on δ_M, the N1 solution showed some signs of becoming insensitive to Re. With P decreasing slowly with increasing Re, both the total kinetic energy and the maximum streamfunction appeared to level off. (It should be noted that for the time dependent solutions barotropic instability leads to the generation of eddy kinetic energy that is far greater than that of the steady solution.) Unfortunately the solutions are sensitive to the dynamic boundary condition. For no slip boundary conditions Ro in the viscous sublayer increased with Re even faster than suggested by simple scaling arguments. As the no slip condition is the proper boundary condition on very small length scales, this result indicates that a proper parameterization of the western boundary viscous sublayer is required for high Re. The model with free slip boundary conditions was more

promising. Simple scaling predicts Ro of the order of R_p, which was not contradicted by the numerical results here.

b. Ageostrophic effects

One cannot rule out the possibility that quasi-geostrophic dynamics are sensitive to frictional closure even in the limit $max(\delta_M, \delta_S) \ll \delta_I \ll 1$ and for no net vorticity input. In this scenario, a more complete model must be considered that includes effects of finite Rossby number and fast time scales. As the Rossby number increases, one anticipates an increasing amount of interaction between the Rossby wave and gravity wave modes (Warn, 1986; Bartello, 1995). These interactions allow for a loss of energy from the balanced (i.e., QG) flow to gravity wave modes, which can cascade energy to the dissipation scales. Hence an adequate parameterization may require explicitly including ageostrophic motions to alleviate the constraints on the energetics.

A final possibility is that the large-scale flow remains sensitive to the details of how subgrid scale effects are parameterized. Ultimately, this may imply the enormous requirement of explicitly resolving all scales of motion.

Acknowledgments. We would like to thank the many people who have helped with this research, especially Glenn Ierley, Vitalli Sheremet, Halldor Bjornsson, Gavin Schmidt, Fred Dupont, Francois Primeau and Evelyn Tsang. Sebius Doedel was very helpful in developing the pseudo-arclengthcode. We also thank both anonymous reviewers for their helpful suggestions. This work was funded by AES, NSERC, and FCAR Quebec.

REFERENCES

Arakawa, A. 1966. Computational design for long-term numerical integration of the equations of fluid motion: Two-dimensional incompressible flow. Part 1. J. Comput. Phys., *1,* 119–143.

Arakawa, A. and V. R. Lamb. 1977. The UCLA general circulation model, *in* Methods in Computational Physics, *17,* Academic Press, 174–265.

Bartello, P. 1995. Geostrophic adjustment and inverse cascades in rotating stratified turbulence. J. Atmos. Sci., *52,* 4410–4428.

Böning, C. W. 1986. On the influence of frictional parameterization in wind-driven circulation models. Dyn. Atmos. Oceans, *10,* 63–92.

Cessi, P., R. V. Condie and W. R. Young. 1990. Dissipative dynamics of western boundary currents. J. Mar. Res., *48,* 677–700.

Cessi, P. and G. R. Ierley. 1995. Symmetry-breaking multiple equilibria in quasi-geostrophic, wind-driven flows. J. Phys. Oceanogr., *25,* 1196–1205.

Dijkstra, H., M. Molemaker, A. Van der Pleg and E. Botta. 1995. An efficient code to compute nonparallel steady flows and their linear stability. Comp. Fluids, *24,* 415–434.

Harrison, D. E. and W. R. Holland. 1981. Regional eddy vorticity transport and the equilibrium vorticity budgets of a numerical model ocean circulation. J. Phys. Oceanogr., *11,* 190–208.

Holland, W. R. 1978. The role of mesoscale eddies in the general circulation of the ocean—numerical experiments using a wind-driven quasi-geostrophic model. J. Phys. Oceanogr., *8,* 363–392.

Ierley, G. R. 1990. Boundary layers in the general ocean circulation. Ann. Rev. Fluid Mech., *22,* 111–142.

Ierley, G. R. and V. A. Sheremet. 1995. Multiple solutions and advection-dominated flows in the wind-driven circulation. Part I: Slip. J. Mar. Res., *53,* 703–737.

Jiang, S., F.-F. Jin and M. Ghil. 1995. Multiple equilibria, periodic and aperiodic solutions in a wind-driven, double-gyre, shallow-water model. J. Phys. Oceanogr., *25,* 764–786.

Kamenkovich, V., V. A. Sheremet, A. R. Pastushkov and S. O. Belotserkovsky. 1995. Analysis of the barotropic model of the subtropical gyre in the ocean for finite Reynolds numbers. Part I. J. Mar. Res., *53,* 959–994.

Legras, B. and M. Ghil. 1985. Persistent anomalies, blocking and variations in atmospheric predictability. J. Atmos. Sci., *42,* 433–471.

Le Provost, C. and J. Verron. 1987. Wind-driven ocean circulation transition to barotropic instability. Dyn. Atmos. Oceans, *11,* 175–201.

Lesieur, M. 1997. Turbulence in Fluids, *in* Fluid Mechanics and Its Applications, 3rd edition, *40,* Kluwer Academic Publishers, 515 pp.

Marshall, J. 1984. Eddy-mean-flow interaction in a barotropic ocean model. Quart. J. R. Met. Soc., *110,* 573–590.

McCalpin, J. D. and D. B. Haidvogel. 1996. Phenomenology of the low-frequency variability in a reduced-gravity, quasi-geostrophic double-gyre model. J. Phys. Oceanogr., *26,* 739–752.

Moro, B. 1988. On the nonlinear Munk model. I. Steady flows. Dyn. Atmos. Oceans, *12,* 259–287.

Munk, W. H. 1950. On the wind-driven ocean circulation. J. Meteorol., *7,* 79–93.

Pedlosky, J. 1987. Geophysical Fluid Dynamics, 2nd edition, Springer-Verlag, Berlin, Heidelberg, New York, 710 + xv pp.

—— 1996. Ocean Circulation Theory, Springer-Verlag, Berlin, Heidelberg, New York, 403 + xi pp.

Press, W. H., S. A. Teukolsky, W. T. Vetterling and B. P. Flannery. 1986. Numerical Recipes: The Art of Scientific Computing, Cambridge University Press, Cambridge, 818 + xx pp.

—— 1992. Numerical Recipes in FORTRAN: The Art of Scientific Computing, 2nd edition, Cambridge University Press, Cambridge, 963 + xxvi pp.

Primeau, F. W. 1998. Multiple equilibria of a double-gyre ocean model with super-slip boundary conditions. J. Phys. Oceanogr., (in press).

Scott, R. B. 1999. Mechanical energy flux to the surface geostrophic flow using TOPEX/POSEIDON data, *in* 23rd EGS General Assembly, Nice, 1998, P. Knudsen and P.-Y. Le Traon, eds., Physics and Chemistry of the Earth, *24,* European Geophysical Society, EGS, (in press).

Seydel, R. 1994. Practical Bifurcation and Stability Analysis: From Equilibrium to Chaos, Interdisciplinary Applied Mathematics, 2nd edition, Springer-Verlag, New York, 407 + xv pp.

Sheremet, V. A., G. R. Ierley and V. Kamenkovich. 1997. Eigenanalysis of the two-dimensional wind-driven ocean circulation problem. J. Mar. Res., *55,* 1–36.

Sheremet, V. A., V. Kamenkovich and A. R. Pastushkov. 1995. Analysis of the barotropic model of the subtropical gyre in the ocean for finite Reynolds numbers. Part II. J. Mar. Res., *53,* 995–1024.

Stammer, D. 1997. Global characteristics of ocean variability estimated from regional TOPEX/POSEIDON altimeter measurements. J. Phys. Oceanogr., *27,* 1743–1769.

Stommel, H. 1948. The westward intensification of wind-driven ocean currents. Trans. Am. Geophys. Union, *29,* 202–206.

Veronis, G. 1966. Wind-driven ocean circulation—Part 2. Numerical solutions of the nonlinear problem. Deep-Sea Res., *13,* 31–55.

Warn, T. 1986. Statistical mechanical equilibria of the shallow water equations. Tellus, *38A,* 1–11.

Received: *18 November, 1997;* revised: *28 July, 1998.*